Performance of a Multibody Point Absorber with a Damper Plate in Irregular Waves

Suman Kumar, Vishnu Vijayasankar, and Abdus Samad

Abstract—Wave energy converters (WECs) behave differently when operating in irregular waves than in regular waves. Although numerous studies have described WEC dynamics in regular waves, the ocean experiences irregular waves, making it essential to evaluate the performance under such conditions. A multibody WEC has mixed motion, adding complexity to system dynamics. In this study, a multibody floating-point absorber WEC equipped with a damper plate was designed and tested for irregular wave conditions in a wave basin at IIT Madras. The wave conditions varied, with significant wave heights ranging from 0.15 to 0.23 m and peak periods from 1 to 2.5 s. Hydrodynamic coefficients such as the Response Amplitude Operator (RAO), excitation force, radiation damping, and added mass were computed using the panel method. A multibody dynamics solver was used to calculate the power absorption. Additionally, a new buoy configuration with a deeper draft was designed and compared with the buoy equipped with a damper plate. The point absorber with a damper plate achieved a maximum power output of 14.05 W at $H_s = 0.23$ m and $T_P = 2.5$ s. The highest absorption efficiency was 48.2% at $H_s = 0.20$ m and $T_P = 2.5$ s.

Index Terms—Damper plate, Hydrodynamic coefficients, Multibody, Point absorber, Power absorption, Wave energy converter.

I. INTRODUCTION

THE oceans serve as reservoirs for solar energy, primarily manifested in the kinetic energy of waves. It is predicted that 40 GW of power can be produced only from the Indian coast [1]. This research aligns with the United Nations Sustainable Development Goals by advancing renewable energy technology, contributing to affordable and clean energy (SDG 7), climate action (SDG 13), and the sustainable use of ocean resources (SDG 14). Among hundreds of different types of wave energy converters (WECs), a floating point absorber (PA) WEC can harness energy from a single point, irrespective of the wave direction [2]. Fig .1 shows a

S. Kumar and A. Samad are with the Wave Energy and Fluids Engineering Laboratory, Department of Ocean Engineering, Indian Institute of Technology Madras, Chennai 600036, India (e-mails: oe22d012@smail.iitm.ac.in , samad@iitm.ac.in).
V. Vijayasankar is with the Department of Naval Architecture and Marine Engineering, University of Michigan, Ann Arbor, MI 48109, United States (e-mail: vishnuvs@umich.edu).
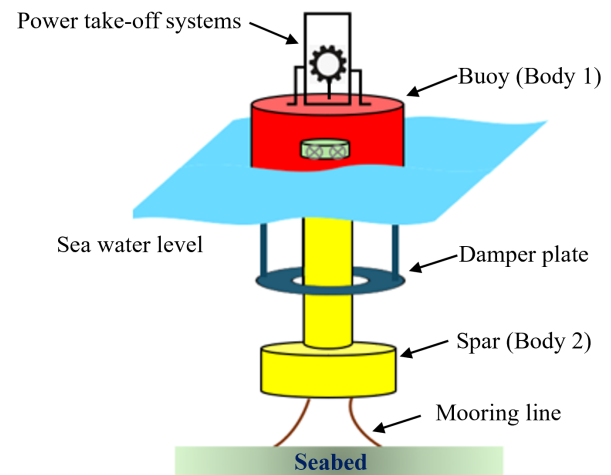
Fig. 1: A PA schematic diagram.

conceptual design of a PA equipped with a damper plate. The PA can operate in either a submerged or floating configuration. Typically, PAs do not require a fixed structure. A mooring line connecting the spar and seabed can maintain the PA stationed.

The PA has a floating cylindrical-shaped buoy, a vertical cylindrical spar, and a power take-off system (PTOS). The spar passes through the buoy and a significant portion remained submerged. During the wave action, the heave motion dominates the buoy, while the spar remains almost stationary. As a result, the buoy and spar create relative motion, which is transferred to a rack and pinion system to rotate the shaft unidirectionally. The unidirectional motion is further transferred to a generator to produce electricity. Instead of rack and pinion, there are other mechanisms to harness energy from the relative motion, such as a hydraulic system coupled with a turbine or linear generator system. In the hydraulic system, a pump delivers water to an elevated location, and the turbine-generator assembly produces electricity from stored water. The mechanism that converts mechanical energy to useful power is called the PTOS. Among the PAs, a single-body or multibody system can be designed. Due to stability constraints and directional limitations, single-body point absorbers exhibit a limited efficiency in capturing wave energy. The multibody analysis is difficult as it requires an understanding of the dynamics of the buoy and spar, individually and combined when harnessing power. Among the PTOS, a linear generator can be a good choice, but it demands specific expertise in design and operation; therefore, in this

study, only a rotary generator was considered. The rotary generator obtains torque through a rack-and-pinion mechanism. When designed optimally, a two-body floating PA operates under a wide range of wave conditions [3].

Recent studies on PAs are presented in table II. The literature shows studies on hydrodynamics, PTOS damping, viscous nonlinear modelling and control. Generator loading also affects the WEC's performance significantly [3]. Flores et al. [4] studied the performance of a floating PA with three distinct float designs off the coast of Ensenada, Baja California, Mexico. Chen et al. [5] analyze the performance of a deformable double-float wave energy converter (DFWEC-AUV) for autonomous underwater vehicles (AUVs). The results show that the optimized DFWEC-AUV can increase the energy capture performance by 4.7 times. Luan et al. [6] studied the numerical verification and validation for a WEC, and the results indicate satisfactory agreement between the numerical and experimental motion displacements. Natarajan and Cho [7] propose a two-body WEC where a torus-shaped outer cylinder follows waves while a heave disk restricts the inner cylinder's motion. This design enhances energy extraction across wave frequencies by leveraging viscous damping. Pavlidou and Angelides [8] optimize a two-body heaving WEC using a genetic algorithm and H^∞ criterion to balance the wave energy extraction and sprung mass isolation. Similarly, much work on hydrodynamics, PTOS damping and geometric and parametric optimizations have been reported in the literature table II. It was found that substantial literature exists on PA under regular and irregular waves, but few on multi-body PA with a damper plate. Kalidoss and Banerjee [9] studied the effect of different float and torus designs on power performance and found that a float with a damper plate was more suitable for longer wave periods.

The present study investigates the hydrodynamic behavior of a multi-body floating PA with attached damper plates [10] under irregular wave conditions and compares its performance to a deeper draft design. The PA's performance under varying wave conditions was evaluated through laboratory tests in a wave basin and numerical modeling based on frequency- and time-domain analyses. The paper outlines the problem definition, experimental and numerical methodologies, followed by results and discussion.

A. Abbreviations and acronyms

TABLE I: Nomenclature and list of symbols.

Abbreviations

AM	Added mass	IRF	Impulse response function
BEM	Boundary element method	PA	Point absorber
BEMIO	Boundary element input/output	PM	Pierson–Moskowitz
DAQ	Data acquisition system	PSD	Power spectral density
DOF	Degree of freedom	PTOS	Power take-off system
EIF	Excitation impulse function	RAO	Response amplitude operator
FFT	Fast Fourier transform	WEC	Wave energy converter

Symbols

A_w	Waterplane area [m^2]	P_{av}	Average absorbed power [W]
$A_z(\infty)$	Added mass at infinite frequency [kg]	P_w	Wave power [W]
$B_z(\omega)$	Radiation damping coefficient [N·s/m]	R	Resistive loading [Ω]
C_{PTOS}	PTO damping coefficient [N·s/m]	$R_f(t)$	Ramp function
$f_{\text{ex,irr}}$	Wave excitation force [N]	$S(f)$	Spectral density [m^2/s]
F_{Ex}	Heave reaction force [N]	t	Simulation time [s]
F_{rad}	Radiation force [N]	T_p	Peak period [s]
g	Acceleration due to gravity [m/s^2]	v_g	Group velocity [m/s]
$\overline{GM}$	Metacentric height [m]	V	Displacement volume [m^3]
H_s	Significant wave height [m]	W	Standard mass [kg]
I_T	Transverse moment of inertia [m^4]	$z(t)$	Heave displacement [m]
K_{PTOS}	PTO stiffness [N/m]	$\dot{z}(t)$	Heave velocity [m/s]
$K_e(t)$	Excitation force impulse function [N·s]	$\ddot{z}(t)$	Heave acceleration [m/s^2]
$K_z(t)$	Radiation force impulse function [N·s]	$\dfrac{dy}{dt}$	Pinion velocity [m/s]
$\overline{KB}$	Height of buoyancy centre [m]	$\dfrac{d^2y}{dt^2}$	Pinion acceleration [m/s^2]
$\overline{KG}$	Height of gravity centre [m]	ρ	Seawater density [kg/m^3]
m_p	Pinion mass [kg]	ω	Wave frequency [rad/s]
M	Buoy mass [kg]	φ	Float inclination angle [rad]

TABLE II: Recent studies on PA.

Author/s	Hydrodynamics	PTOS Type	PTOS Damping	Resistive Loading
Flores et al. [4]	✓	Mechanical	✗	✗
Chen et al. [5]	✓	Ball screw mechanism	✓	✗
Luan et al. [6]	✓	–	✗	✗
Natarajan and Cho [7]	✓	Linear PTOS	✓	✗
Ding et al. [11]	✓	–	✓	✗
Yang et al. [12]	✓	Hydraulic	✗	✗
Masoomi et al. [13]	✓	–	✗	✗
Chen et al. [5]	✓	Mechanical	✓	✗
Shabara and Abdelkhalik [14]	✓	Linear damping system	✗	✗
Yu et al. [15]	✓	Rack and pinion	✓	✗
Lande-Sudall et al. [16]	✓	Linear damper	✓	✗
Jalani et al. [17]	✓	–	✓	✗
Pavlidou and Angelides [8]	✓	Linear PTOS	✓	✗
Rahimi et al. [18]	✓	Spring-damper	✓	✗
Li et al. [19]	✓	Mechanical Motion Rectifying PTOS	✓	✗
Rusch et al. [20]	✓	–	✗	✗
Giorgi et al. [21]	✓	–	✗	✗
Meng et al. [22]	✓	Linear generator	✓	✗

II. WAVE BASIN TESTING OF THE PA

A. PA

In this study, a cylindrical buoy with an attached damper plate is designed fig. 2a. According to Vijayasankar et al. [10], adding a damper plate to the floating buoy of a PA increases its added mass and reduces its natural frequency in the heave mode, thereby improving its performance in realistic wave periods without increasing the volume and size, respectively. A spar connected to the mooring lines passes through the buoy and damper plate and is connected to the PTOS. The buoy with damper plate (F1A) has a diameter of 0.6 m, a height of 0.4 m, and weighs 35 kg, while the spar measures 2 m long (fig. 2b). A second buoy configuration with a deeper draft (F1B) of 0.3 m was designed while maintaining a 0.6 m diameter to ensure consistent hydrostatic stiffness. A ballast mass of 60 kg was selected through iterative adjustments to match the natural frequency of the F1A. This design allows for a direct comparison of the hydrodynamic performances of F1A and F1B, focusing on resonance-tuning and power-absorption efficiency. The detailed dimensions are outlined in the table III. The manufacturing process took place in a nearby facility and a central workshop at IIT Madras. Subsequently, the system was tested in the wave basin at the Department of Ocean Engineering, IIT Madras.

The PTOS comprises a pair of pinions with a free-wheel mechanism welded together (fig. 2c) to allow smooth rotation of the gear teeth while the inner cage of the freewheels remains fixed. The wheels share a common shaft. Two vertical racks were connected to a buoy, and each rack was meshed with one pinion. The pinion cage was attached to the spar. As the buoy moved, the pinion rotated along the racks, providing unidirectional motion to the shaft. The shaft is connected to a DC generator to produce electricity.

B. Wave basin

The wave basin is square-shaped with dimensions of 30 m × 30 m and has a water depth of 3 m, as shown in fig. 3. Equipped with a wave absorber to minimize reflection effects and 52 synchronized pedals that act as actuators, it can generate both regular and irregular waves. During the generation of irregular waves, the wave field simulator MIKE21 managed significant wave heights for statistical uncertainties for zero-crossing periods.

C. Experimental procedure

The damping of the PTOS was verified before testing the PA in a wave basin. Most damping arises due to friction in the sliding and rotating components. Damping affects energy extraction efficiency and system stability. A dry bench test was conducted to investigate the damping characteristics of the PTOS. The total damping of the PTOS is influenced by both external and internal factors, including the resistance within the generator and mechanical friction. The preliminary damping of the PTOS was estimated for various resistive loads. The pinion was connected to one end of a steel wire passing over the pulley, and the other end was connected to the standard weight to replicate wave loads, as illustrated in fig. 4. An accelerometer is attached to the pinion cage. The accelerometer data were processed to obtain the corresponding velocity values, which were essential for determining the damping characteristics (eq. (1)). Resistors with different ratings were connected across the generator output to examine their effect on PTOS's damping of the PTOS.

To calculate PTOS-damping coefficients (C_{PTOS}), the expression can be used as (fig. 4):

$$(W + m_p)\frac{d^2y}{dt^2} + C_{PTOS}\frac{dy}{dt} = (W - m_p)g \quad (1)$$

where W and m_p denote the standard weight (in kg) and pinion mass, respectively; and $\frac{d^2y}{dt^2}$ and $\frac{dy}{dt}$ denote the acceleration and velocity of the pinion, respectively.

Initially, the buoy was placed in water to check for the natural period through a decay test. A decay test involves displacing the buoy from its equilibrium position and releasing it to measure its natural period

(a) Buoy with heave plate (b) Spar (c) Rack and pinion PTOS
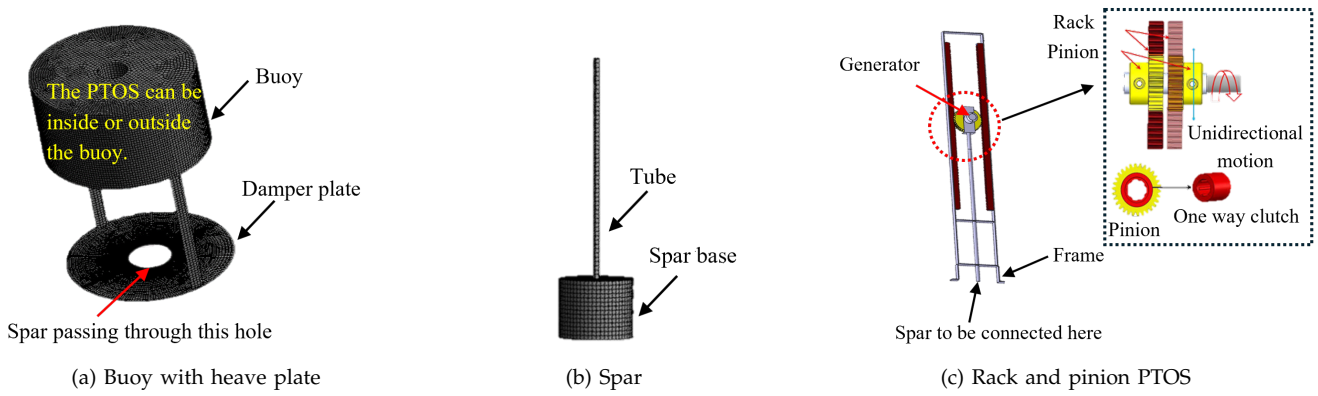
Fig. 2: Components of the PAWEC system: (a) Buoy with heave plate, (b) Spar, and (c) Rack and pinion PTOS.

Fig. 3: Wave basin facility at IIT Madras.

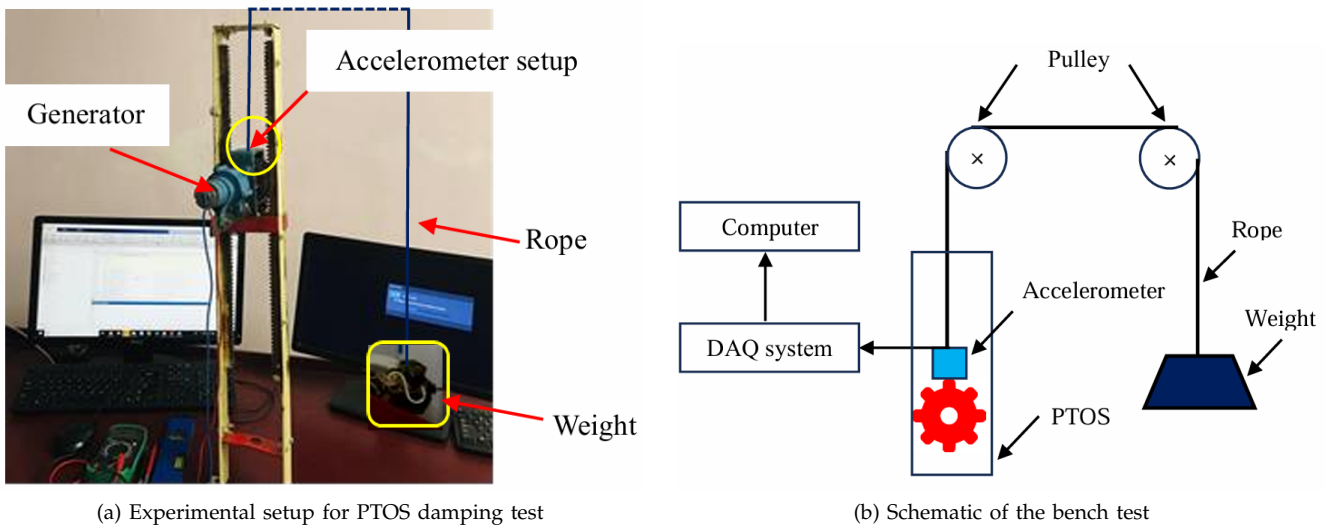(a) Experimental setup for PTOS damping test (b) Schematic of the bench test

Fig. 4: Dry bench test setup: (a) Experimental setup for PTOS damping test, (b) Schematic of the bench test.

and damping characteristics based on its oscillatory motion as it returns to equilibrium. Irregular waves were generated using the Pierson-Moskowitz (P-M) spectrum, which describes the distribution of wave energy across different frequencies in a fully developed sea. Considering the operational limitations of the wave basin, the test was conducted for various combinations of peak periods (T_p) ranging from 1 -2.5 s and the significant wave height (H_s) ranging from 0.15

- 0.23 m with the model using a scale factor of $1 : 3.3$. By applying Froude scaling, these model wave heights correspond to 0.50 to 0.76 m in full-scale conditions, while the wave periods range from 1.8 to 4.5 s.

Wave elevations, heave accelerations, and heave reaction forces were measured using different sensors. A data acquisition (DAQ) system, such as Spider 8 (fig. 7d), transfers the data to a computer. The experimental setup layout in the wave basin is shown in

TABLE III: Experimental setup parameters.

Description	Value	Unit
Wave tank		
Dimensions	30×30	m
Water depth	3	m
PA position from wavemaker	15	m
Buoy (F1A)		
Diameter	0.6	m
Height	0.4	m
Wall thickness	0.002	m
Mass	35	kg
Buoy (F1B)		
Diameter	0.6	m
Height	0.6	m
Ballast mass	60	kg
Total mass	90	kg
Spar (F2)		
Outer diameter (Tube)	0.048	m
Thickness (Tube)	0.003	m
Spar base diameter	0.5	m
Length	2	m
Sensors		
Accelerometer	Range: ± 5 g pk; Sensitivity: 1000 mV/g	–
Load cell capacity	3000	N
Wavemeter / Wave Gauge	Type: Conductive; Resolution < 1 mm	–
DAQ (Spider8)	Resolution: 16 bits	–
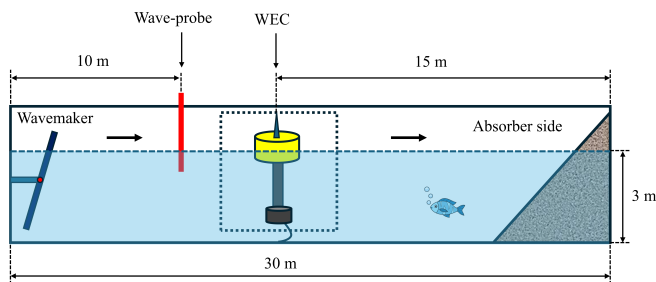
Fig. 5: Wave tank test setup.

fig. 5. A floating structure remains in static equilibrium if the total force and moment acting on it are zero. A floating device is stable if the metacentre lies above the centre of gravity (fig. 6a) [23]. Initial metacentric height $(\overline{GM})$ is defined as:

$$\overline{GM} = \overline{KB} + \frac{I_T}{V} - \overline{KG} \qquad (2)$$

where $\overline{KB}$, $\overline{KG}$, I_T and V denote the height of the buoyancy centre, gravity centre, and transverse moment of inertia about the waterline and the displaced volume, respectively.

Fig. 6b shows a static stability curve for a floating symmetric device, $GM > 0$. For considerable inclination angles and complex geometries, the pressure surface integrals obtained by numerical analysis can be used to define the stability of the floating device. Considering the PA as an axisymmetric device, point B is vertically below G. The PA was designed to withstand the forces of waves, currents, and winds. The mooring analysis was not included in the present study, as the primary focus was to investigate the influence of the damper plate on the hydrodynamic performance. The PA in the wave basin during the experiment is shown in the fig. 7.
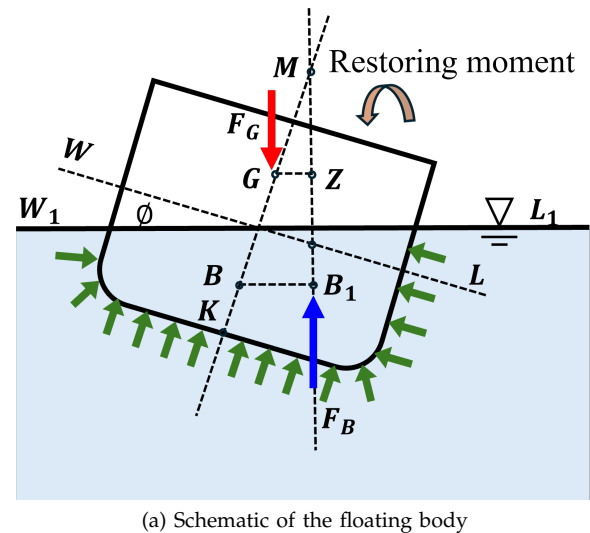
(a) Schematic of the floating body
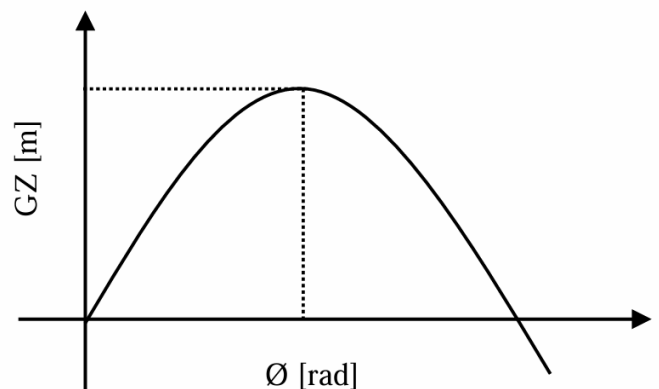
(b) Static stability curve

Fig. 6: Stability of the floating body: (a) schematic of the floating body, (b) static stability curve.

(a) S-type load cell mounting

(b) Accelerometer setup

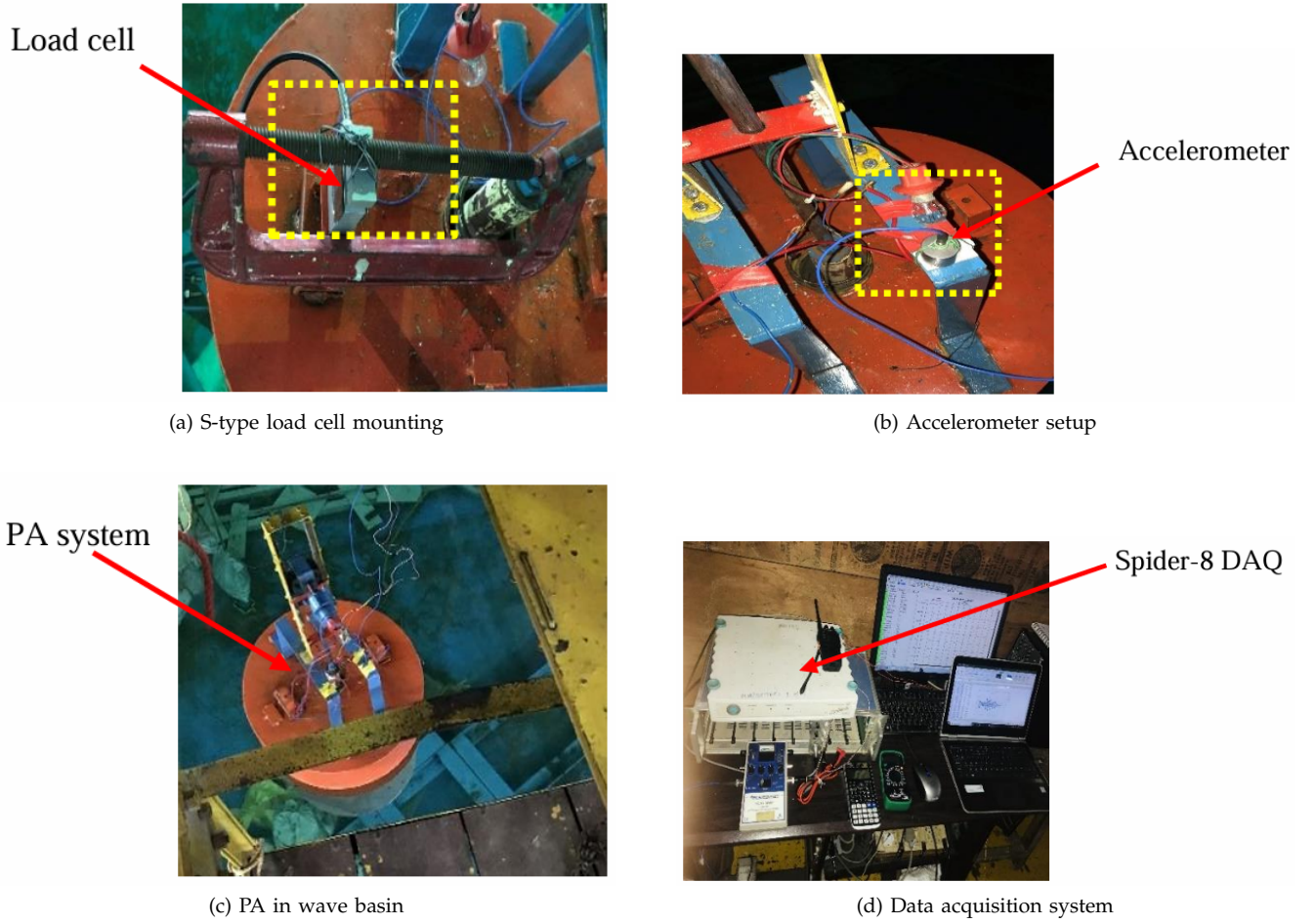
(c) PA in wave basin

(d) Data acquisition system

Fig. 7: Experimental setup: (a) S-type load cell mounting, (b) accelerometer setup, (c) PA in wave basin, and (d) data acquisition system.
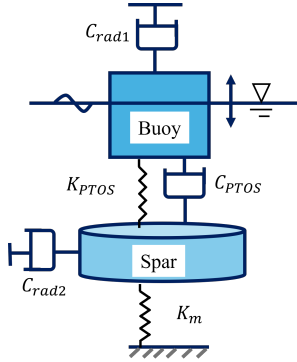

Fig. 8: Spring–mass–damper model.

III. MATHEMATICAL FORMULATION

A. The motion equation

A multibody PA is modeled as a spring-mass-damper system, as shown in fig. 8. A PTOS can be represented as a spring-damper system by assigning appropriate stiffness and damping values.

The equation of the heave motion of the float for a linear WEC is expressed as [24],

$$\left[A_z(\infty) + M\right]\ddot{z}(t) + \int_0^t k(\tau)\dot{z}(t - \tau)\,d\tau + C_{\text{PTOS}}\dot{z}(t)$$

$$+ (\rho g A_w + K_{\text{PTOS}})z(t) = f_{\text{ex,irr}} \tag{3}$$

where $A_z(\infty)$ and $k(\tau)$ denote the limiting value of the added mass at an infinite frequency ($\omega \to \infty$) and the time-dependent kernel function, respectively. A_w and $f_{\text{ex, irregular}}$ denote the water plane area and the wave excitation force in irregular waves, respectively.

The Convolution term in eq. (3) indicates the fluid memory effect in the radiation force, which is given as:

$$k_z(t) = \frac{2}{\pi} \int_0^\infty B_z(\omega) \cos \omega t \, d\omega \tag{4}$$

where $k_z(t)$ is the radiation impulse function (IRF), and $B_z(\omega)$ is the radiation damping coefficient.

The radiation force can be expressed as:

$$F_{\text{rad}} = -A_z(\infty)\dot{z}(t) - \int_0^\infty k_z(t - \tau)\dot{z}(\tau)\,d\tau \tag{5}$$

The wave excitation force was calculated using a ramp function ($R_f(t)$) to prevent strong transient flows during the early stages of the simulation. The ramp function [25] is defined as:

$$R_f(t) = \begin{cases} \frac{1}{2}\left(1 + \cos\left(\pi + \frac{\pi t}{t_r}\right)\right) & t/t_r < 1 \\ 1 & t/t_r \geq 1 \end{cases} \tag{6}$$

where t and t_r represent the simulation and ramp times, respectively.

The wave excitation force of floating bodies in irregular waves can be obtained by superimposing regular wave components with different frequencies as follows:

$$F_{\text{exc}}(t) = \mathfrak{Re} R_f(t) \sum_{j=1}^{N} F_{\text{exc}}(\omega_j, \theta) e^{i(\omega_j t + \varphi_j)} \sqrt{2S(\omega_j)\Delta\omega_j}$$

(7)

Here, φ refers to a random phase angle and N is the number of frequency bands chosen to discretize the wave spectrum. Each regular wave component is derived from the wave spectrum $S(\omega)$. F_{exc} is a complex wave excitation vector that depends on the frequency and θ represents the wave direction.

In addition, the excitation force impulse response function (EIF), as given by [24], is

$$K_e(t) = \mathfrak{Re}\left[\frac{1}{2\pi}\int_{-\infty}^{\infty} F_{\text{exc}}(\omega, \theta)e^{i\omega t}\, d\omega\right]$$

(8)

where $\mathfrak{Re}$ denotes the real part of the equation.

B. Pierson–Moskowitz (PM) spectrum

In the frequency domain, the wave spectrum represents a linear superposition of regular waves with different amplitudes and periods. The PM spectrum is used for a fully developed sea, where wave growth is unrestricted by the fetch. This spectrum is characterized by the peak wave frequency and significant wave height. Given that the device being studied is axisymmetric and independent of the wave direction, a one-dimensional spectrum is sufficient for the analysis. The PM spectrum was used to generate irregular waves in both the experimental and numerical simulations. The PM spectrum is widely used in the offshore industry to describe fully developed seas, and its parameters depend strongly on the wind speed, fetch, wind direction, and storm front locations. It is defined as [26]:

$$S_{PM}(f) = \frac{H_{m0}^2}{4}(1.057 f_h)^4 f^{-5} \exp\left[-\frac{1}{4}\left(\frac{f}{f_h}\right)^4\right]$$

(9)

The time-averaged of available wave power for a given irregular sea state can be determined using,

$$P_w = \rho g \int_0^{\infty} S_{PM}(f)c_g(f)df$$

(10)

In the above expressions, f represents the wave frequency, and c_g denotes the group velocity of the wave. The group velocity of regular waves can be assigned at each frequency used to derive the sea spectrum.

IV. NUMERICAL ANALYSIS

The multibody PA oscillates and creates a wave-structure interaction problem. Diffraction and radiation problems were solved using a Boundary Element Method (BEM) code available in [27]. Physical parameters such as weight and volume were defined based on the experimental model. Furthermore, a multibody open-source code, WEC-Sim [25] analyzed the system in the time domain and evaluated the performance
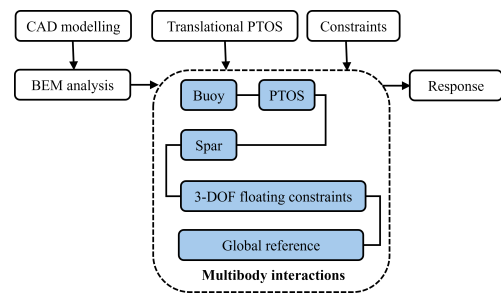

Fig. 9: Modelling flow process.

parameters using the frequency-domain hydrodynamic coefficient obtained from the BEM analysis. The simulation results include the absorbed power and capturing efficiency. The numerical results were compared with the results of the wave basin test.

The numerical modelling flow process is shown in fig. 9. To enable multi-body interactions, the systems were analyzed using the multi-body dynamics solver Simscape Multibody in MATLAB/Simulink. The hydrodynamic coefficients obtained from the BEM code are fed into the boundary element input/output (BEMIO) code. The BEMIO code calculates the time-dependent radiation and excitation impulse functions. The functions calculate the respective forces using the convolution integral eq. (4) and eq. (8). Finally, the forces along with the wave class, spectrum type, mass properties, and PTOS damping/stiffness were used as the input parameters for the analysis. The simulations were run for H_s =0.15, 0.20, and 0.23 m, with peak periods ranging from 1 to 2.5 s, at a water depth of 3 m to match the experimental conditions. The 4th-order Runge-Kutta integration scheme was used to produce time-domain solutions.

V. RESULT AND DISCUSSION

A. Radiation and excitation impulse function

The normalised radiation (IRF) and excitation impulse response force functions (EIF), obtained from numerical simulations for the heave motion of two floating structures, a buoy (F1A), and a spar (F2), are given in fig. 10a and fig. 10b respectively. IRF measures how the heave motion responds to an impulse force at time $t = 0$. IRF reflects the dynamic characteristics of the structure, including damping, stiffness, and oscillatory behavior. The IRF for the F1A exhibits damped oscillatory behavior, starting with a significant initial response and gradually damping out over time. The F2 shows a much smaller and less oscillatory response, indicating a different dynamic characteristic than that of the F1A. EIF measures the effect of the impulse excitation force on the heave motion of the structure. Unlike the IRF, which captures the system's inherent response to an impulse, the EIF describes the effect of an external impulse force on the system's motion, reflecting how the structure dynamically reacts to sudden excitations such as wave loads. The EIF for the F1A shows a sharp peak at $t = 0$, indicating a strong immediate response to the impulse force, followed by damped oscillations, and the F2 shows a smaller, more
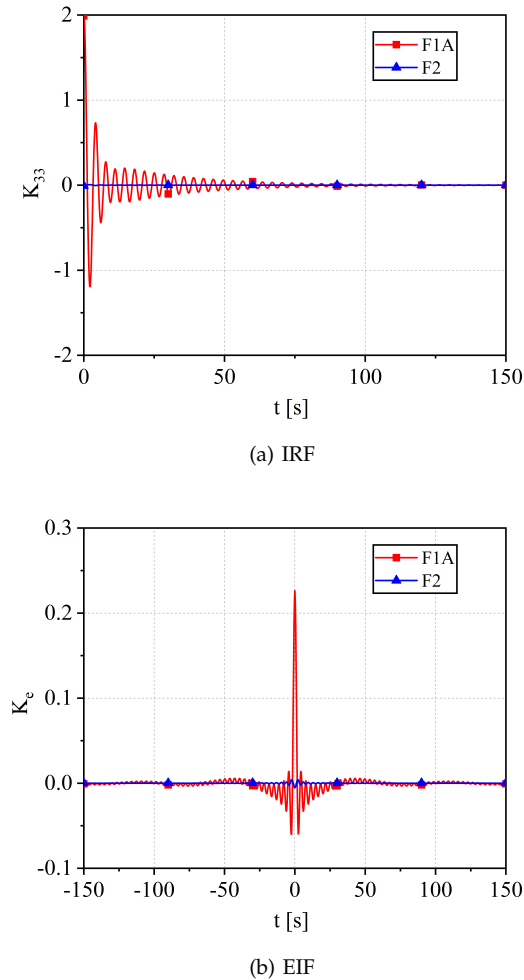
(a) IRF

(b) EIF

Fig. 10: Normalized radiation and excitation impulse functions: (a) IRF and (b) EIF.

stable response, indicating that the F2 is less sensitive to impulse forces than the F1A. The F1A exhibited a more pronounced dynamic response in both the IRF and EIF, characterized by higher amplitude oscillations that gradually dampened over time. The F2 showed a more restrained response with less oscillation and quicker damping, suggesting that it may be more stable in heave motion than the F1A. IRF tends to zero over time, indicating that the system is stable and returns to equilibrium after an impulse disturbance.

In fig. 10, K_{33} and K_e denote the normalized radiation and excitation impulse function values, respectively.

B. Frequency domain hydrodynamic co-efficient

The hydrodynamic coefficients obtained from the BEM analyses are plotted as fig. 11. The RAO describes the motion response of the bodies and incident wave amplitude. Fig. 11a shows the RAO plot for the buoy with damper plate (F1A) and the spar (F2). The F1A heaves freely at a lower frequency ($\sim$ 0–3 rad/s), and peaks at approximately 4.2 rad/s. The RAO decreases with an increase in the wave frequency, and becomes zero for $\omega > 10$ rad/s. This was because of the natural frequency of the F1A. When the incident wave

frequency matched the F1A's natural frequency, the response was maximized, leading to a peak in the RAO plot.

As the wave frequency deviates from the natural frequency, the response decreases; for frequencies much higher than the natural frequency, the response becomes negligible. The F2, which is a long, slender structure, remains in a free state up to a frequency of 1 rad/s, and its response decreases with an increase in frequency. This may be due to the inertia of the F2 and the damping effect of the surrounding water, which tends to suppress its motion at higher frequencies. Fig. 11b shows the normalized excitation force ($F_{\text{ex}}/[\rho * g] : 0°$) at a zero-degree incident angle as a function of wave frequency. The Froude-Krylov and diffraction forces together provide an excitation force [28]. Meanwhile, the forces on the F2 initially increased with frequency and then decreased gradually. The force on the F1A is relatively higher than that on the F2 for a wider frequency range because the F2 is less affected by the incident waves, as it is below the free water surface. The radiation force imposed on hydrodynamic bodies considers radiation damping to be an important index. At zero frequency (no wave), F2 has an almost zero damping coefficient (fig. 11c). With an increase in the frequency, the damping coefficient of F1A initially increases; however, it decreases after reaching a peak. The radiation damping coefficient was lower for the F2 than for the F1A, because the F2 had a low effect on the incident waves. This behavior can be attributed to the body's response to the wave frequency, with the damping coefficient increasing and converging to a constant value at high frequencies, while the radiation wave damping decreases [29]. Along with the heaving bodies, the water particles also move in the fluid domain, contributing to additional mass known as added mass (AM). This has a significant effect on the inertial forces of the system. The AM depends on frequency, as shown in fig. 11d. For F1A, the AM decreases with frequency up to 8 rad/s, after which it becomes constant. This is due to the drainage hole in F1A. F2 has little effect on AM due to its small response. In this study, only the AM from the heave motion is considered. In fig. 11d, A_m denotes the frequency-dependent added mass.

C. Dry-bench test

A bench test was performed on the PTOS system, and the results were plotted. PTOS damping is inversely proportional to the resistive load, as shown in fig. 12. The damping coefficients represent the total damping of PTOS. As the resistive load increases, the generator speed increases, which causes a reduction in the internal damping of the generator [30], although the damping caused by the mechanical friction remains constant. The curve depends on generator characteristics. The bench test yielded different damping values under the various test conditions. Softer damping enables the system to produce large strokes, even for small-wave undulations, without capturing energy. A very high value suppresses buoy movement

(a) RAO

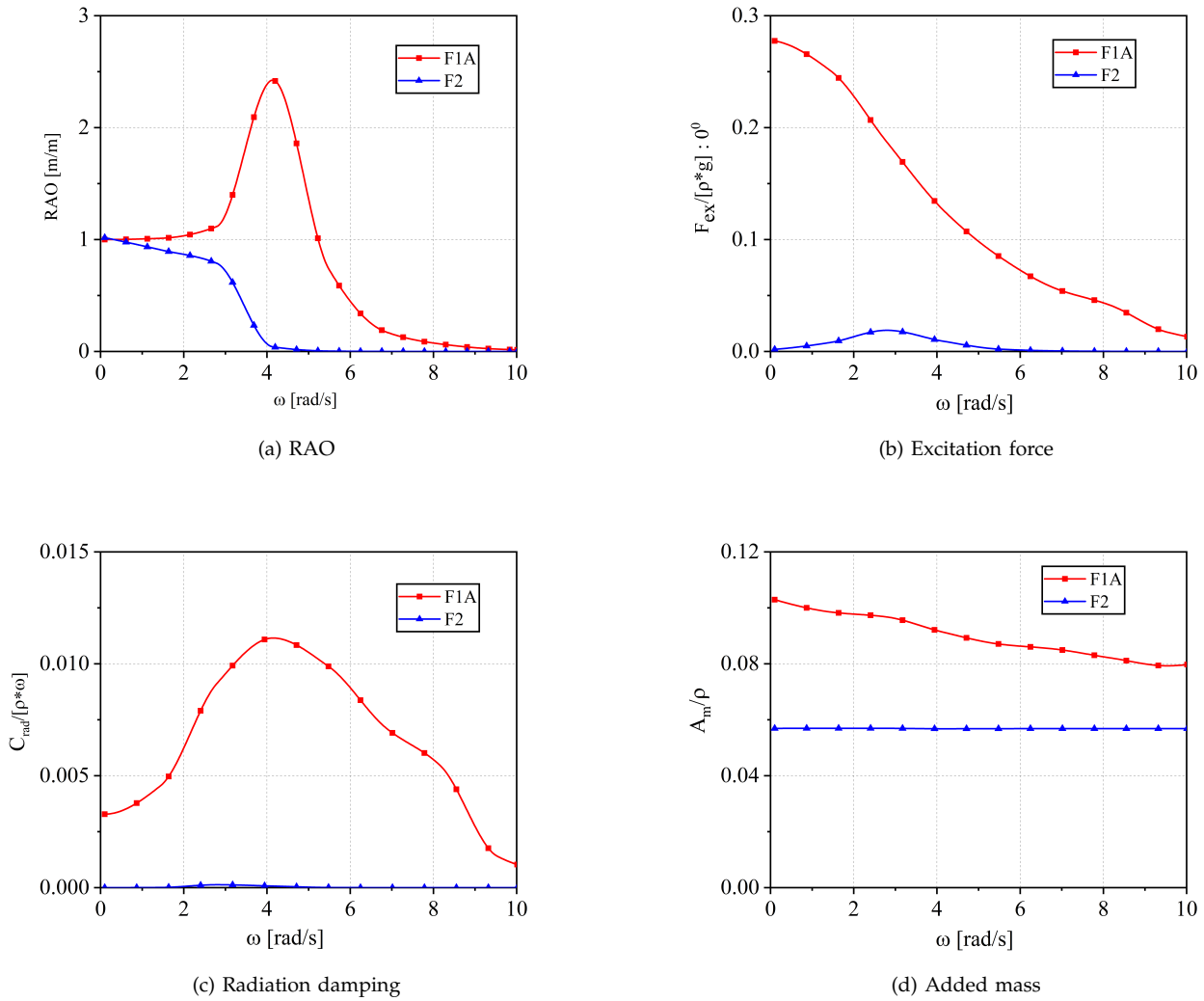(b) Excitation force

(c) Radiation damping

(d) Added mass

Fig. 11: Scaled hydrodynamic coefficients: (a) RAO, (b) excitation force, (c) radiation damping, and (d) added mass.

and prevents it from absorbing energy. Further analyses were performed using numerical modelling. This load-damping curve can be useful in the design of wave energy converters for efficient energy extraction. From the curve (fig. 12), the optimal damping value corresponding to the resistive load can be identified. This provides practical guidance for selecting PTOS damping.

D. Comparison of a buoy with a damper Plate (F1A) and a deeper draft buoy (F1B)

The hydrodynamic performance and power absorption of the buoy equipped with a damper plate (F1A) were compared to those of a buoy with a deeper draft (F1B) but without a damper plate. This comparison was conducted to understand the trade-offs between the two designs and to determine the benefits of incorporating a damper plate over modifying the draft.

RAO results (fig. 13a) show that F1A exhibits a higher peak response, indicating a better resonance tuning. Its added mass (fig. 13b) remains higher across
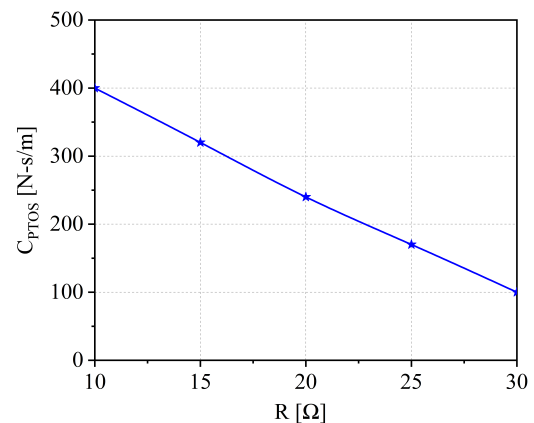
Fig. 12: Variation of PTOS damping with resistive loading.

all frequencies, lowering its natural frequency to align with characteristic wave periods. Conversely, F1B has lower added mass across all frequencies, limiting its
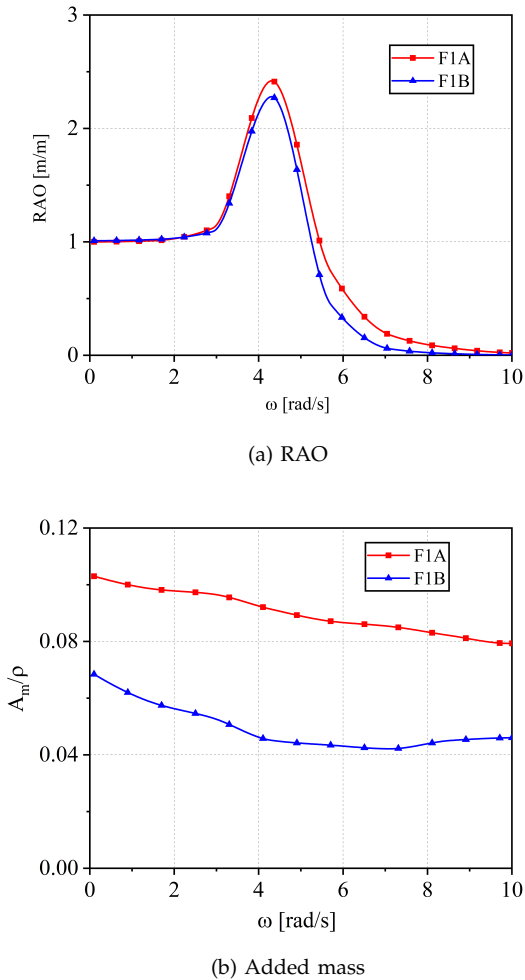
(a) RAO

(b) Added mass

Fig. 13: Scaled hydrodynamic coefficients: (a) RAO and (b) added mass.

resonance performance, although both designs have similar natural periods.

The damper plate increases the added mass, while F1B requires additional ballast to achieve the same natural period. Both designs exhibit similar response bandwidths near resonance, but F1A achieves a higher peak RAO (fig. 13a). While F1B offers a simpler and potentially more cost-effective structure, it compromises power absorption and stability under extreme conditions. The damper plate improves stability and resonance tuning with minimal added complexity, making it well-suited for compact wave energy converters. Fig. 14 confirms that F1A achieves higher power absorption for most of the sea states due to improved resonance tuning and added mass, demonstrating the advantages of a damper plate over increased draft.

E. The influence of PTOS damping in maximising average power output

Fig. 15 illustrates the influence of PTOS damping on maximising the average power output derived from numerical simulations. The PA performs best at the optimal PTOS damping. A lower damping value enables the system to move freely; however, a higher value restricts its motion. It is evident from fig. 15a that for

a peak period of 2.5 s, the average power absorption initially increases with damping, then decreases, and reaches a maximum at a damping value of 100 N-s/m. This shows that the power absorbed by the PTOS for any peak period is dependent on the damping value, which must be carefully studied before choosing the most suitable value for further experimentation. Fig. 15b also shows a decreasing trend in P_{av} across all T_p values for C_{PTOS} greater than 100 N-s/m.

It was noted that the most suitable damping value corresponding to each peak period and significant wave height for maximum average power absorption is 100 N-s/m at 50 to 300 N-s/m. For $H_s = 0.23$ m and $T_p = 2.5$ s, it is evident from the fig. 15c that the system absorbs a maximum P_{av} of approximately 15 W at a C_{PTOS} of 100 N-s/m. For this reason, the same PTOS damping was maintained during wave basin testing by choosing an appropriate resistive loading.

F. Wave reaction force

Experiments were conducted to investigate the reaction force in heave motion only. The present load study focused on the buoy, as it was subjected to a wave load. The vertical reaction force is the result of the wave diffraction force and Froude-Krylov force. The reaction load response time series under different sea states are plotted in fig. 16. The response is irregular as it is subjected to irregular waves. The plot shows that the peak reaction load does not increase monotonically with wave height due to wave irregularity. The PA reacts more to higher-period waves. The peak heave reaction force is 360 N at $H_s = 0.23$ m and $T_P = 2.5$ s. Understanding the reaction load curve can help to assess the structural integrity of the PA, allowing for material selection and reinforcement strategies.

G. Power capture and absorption efficiency

Fig.17 shows the energy absorption efficiency of the PA in different sea states. The ratio of average power absorbed by the PA and the available wave power provides the absorption efficiency. The time average of the velocity was used to determine the power absorbed by PA. During the experiments, the PTOS damping (C_{PTOS}) was controlled to a value of 100 N-s/m by selecting suitable external resistive loading. The available wave power increased with wave height. The resonances were different for different T_P and H_s values. The maximum average power is 14.05 W at $H_s = 0.23$ m, $T_P = 2.5$ s, and $C_{PTOS} = 100$ N-s/m. The peak power for $H_s = 0.23$ m was greater than 14 W for a longer period, which was not captured because the maximum $T_P = 2.5$ s was considered during the experiments due to wave basin limitations.

H. Relative heave response

The relative heave displacement responses of the buoy and spar obtained from the wave basin tests are shown in fig. 18. Measurements were taken for different combinations of significant wave heights and peak periods under irregular wave conditions using
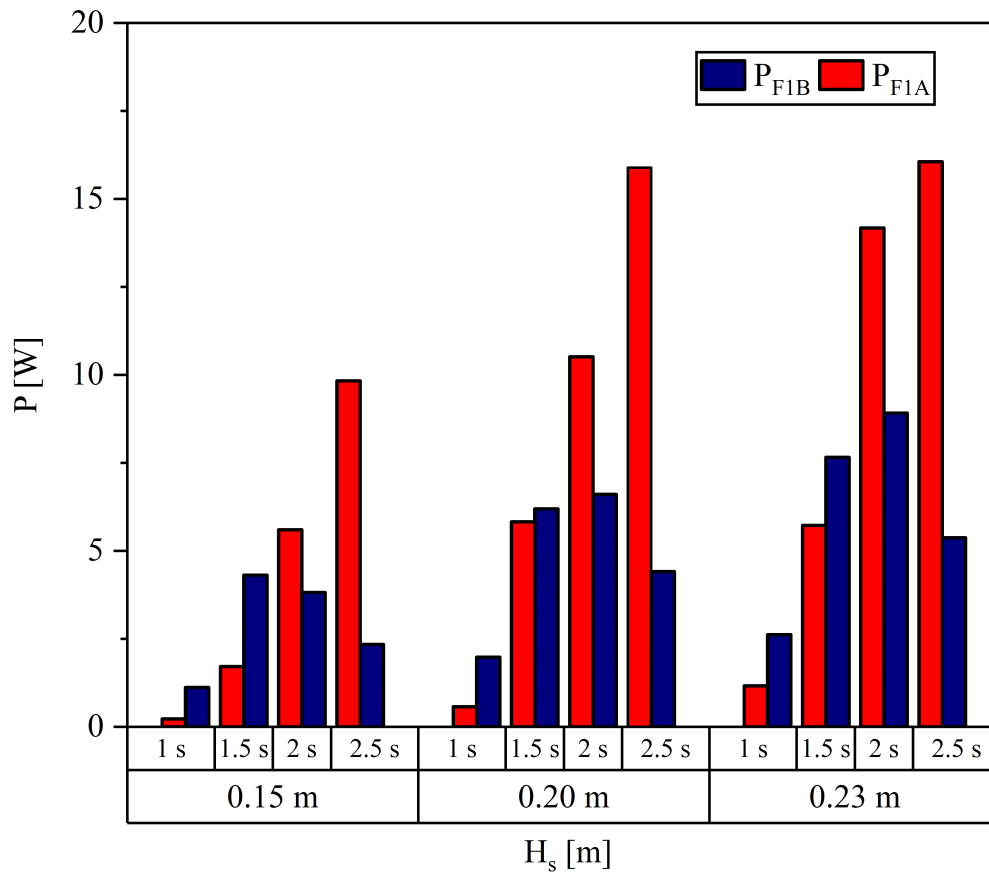
Fig. 14: Comparison of absorbed power for F1A (damper plate) and F1B (deeper draft) across varying significant wave height (H_s) and peak period (T_p).

an accelerometer. The acceleration data were integrated twice with respect to time to obtain the displacement. The accelerometer was calibrated to minimise offsets and prevent error accumulation over time. The heave response of the buoy and spar depends on the hydrodynamic damping, natural period of the system, and wave-induced forces. A large heave amplitude may cause severe damage to the PAWEC. Hence, the hydrodynamic response of the buoy was optimised by selecting a suitable PTOS damping and addressing the damper plate.

Fig. 18 shows the motion characteristics of the PAWEC under the action of an irregular wave. A higher relative response is expected when the wave period approaches the natural period associated with a particular mode shape of a multibody system. As the response is completely random, it is difficult to conclude anything about the power absorption ability of the PAWEC from the response graph. Consequently, irregular responses are best represented by a spectrum. Fast Fourier transform (FFT) was used for efficient conversion. The power absorbed is evaluated by plotting the power spectral density (PSD) function against the frequency, which is described in the following section.

The power spectral density curve is shown in fig. 19 for different combinations of the peak period and significant wave height. The peak in the curve indicates

the maximum energy absorption, corresponding to the abscissa frequency. The obtained spectrum was a multipeak spectrum. The multipeak spectrum arises owing to the interaction of different wave components at varying frequencies, causing multiple resonances in the system. It is evident from the graph that the dominant response in all cases occurs for T_P = 2.5 s, and shorter peak periods show smaller responses across all wave heights (H_s = 0.15 m, 0.20 m, and 0.23 m).

*I. Numerical vs. experimental power comparison and standard deviation*

Fig. 20 shows a good agreement between the numerical and experimental average absorbed power. The numerical simulation was over-predicted because the viscous and nonlinear effects were not considered. Future studies will aim to include viscous effects in numerical modelling to improve the accuracy of the simulations.
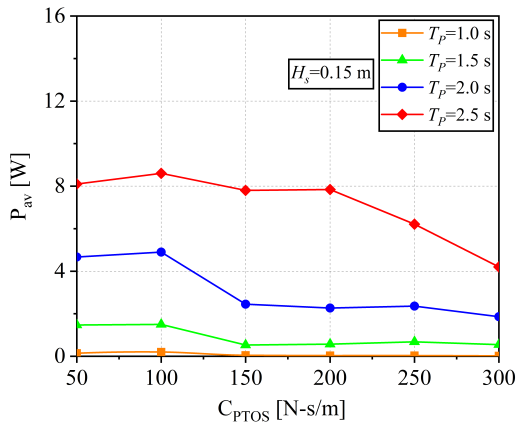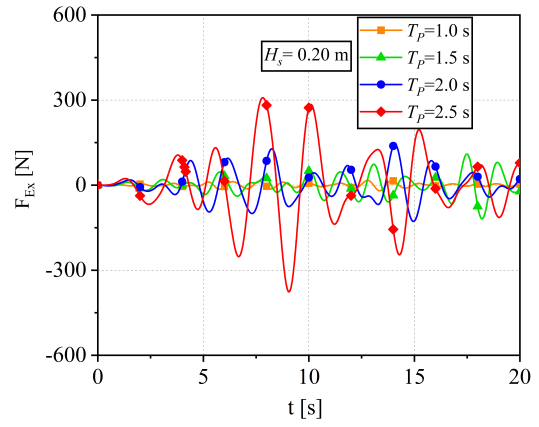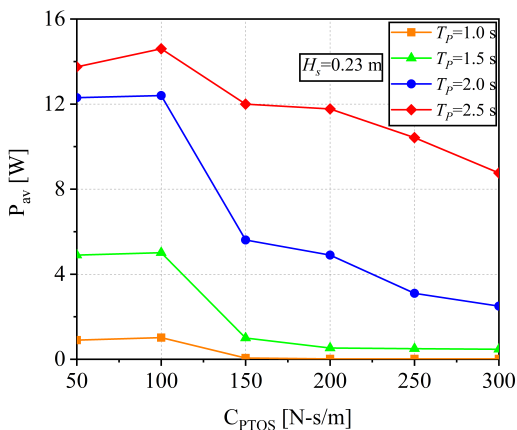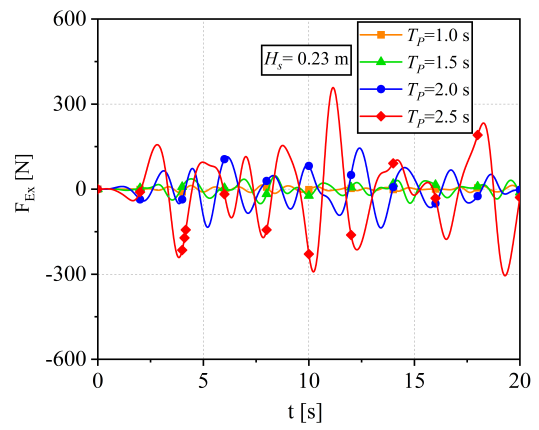
(a) $H_s = 15\,\mathrm{cm}$
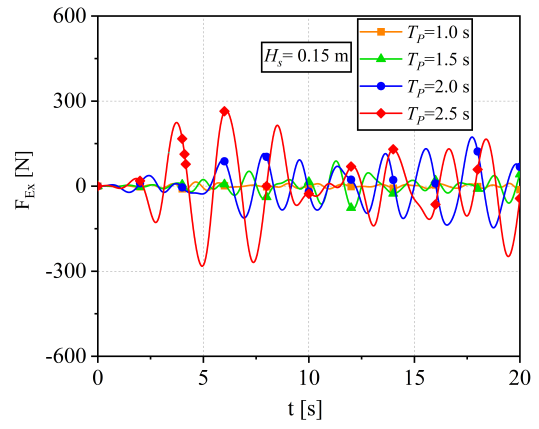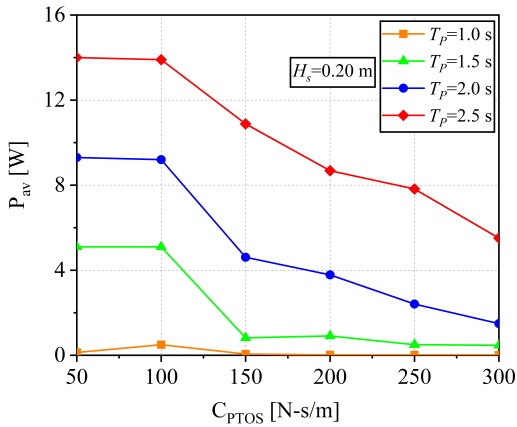
(b) $H_s = 20\,\mathrm{cm}$

(c) $H_s = 23\,\mathrm{cm}$

Fig. 15: Variation of average absorbed power with PTOS damping for different wave heights: (a) $H_s = 15\,\mathrm{cm}$, (b) $H_s = 20\,\mathrm{cm}$, and (c) $H_s = 23\,\mathrm{cm}$.

(a) $H_s = 15\,\mathrm{cm}$

(b) $H_s = 20\,\mathrm{cm}$

(c) $H_s = 23\,\mathrm{cm}$

Fig. 16: Variation of heave excitation force for different wave heights: (a) $H_s = 15\,\mathrm{cm}$, (b) $H_s = 20\,\mathrm{cm}$, and (c) $H_s = 23\,\mathrm{cm}$.
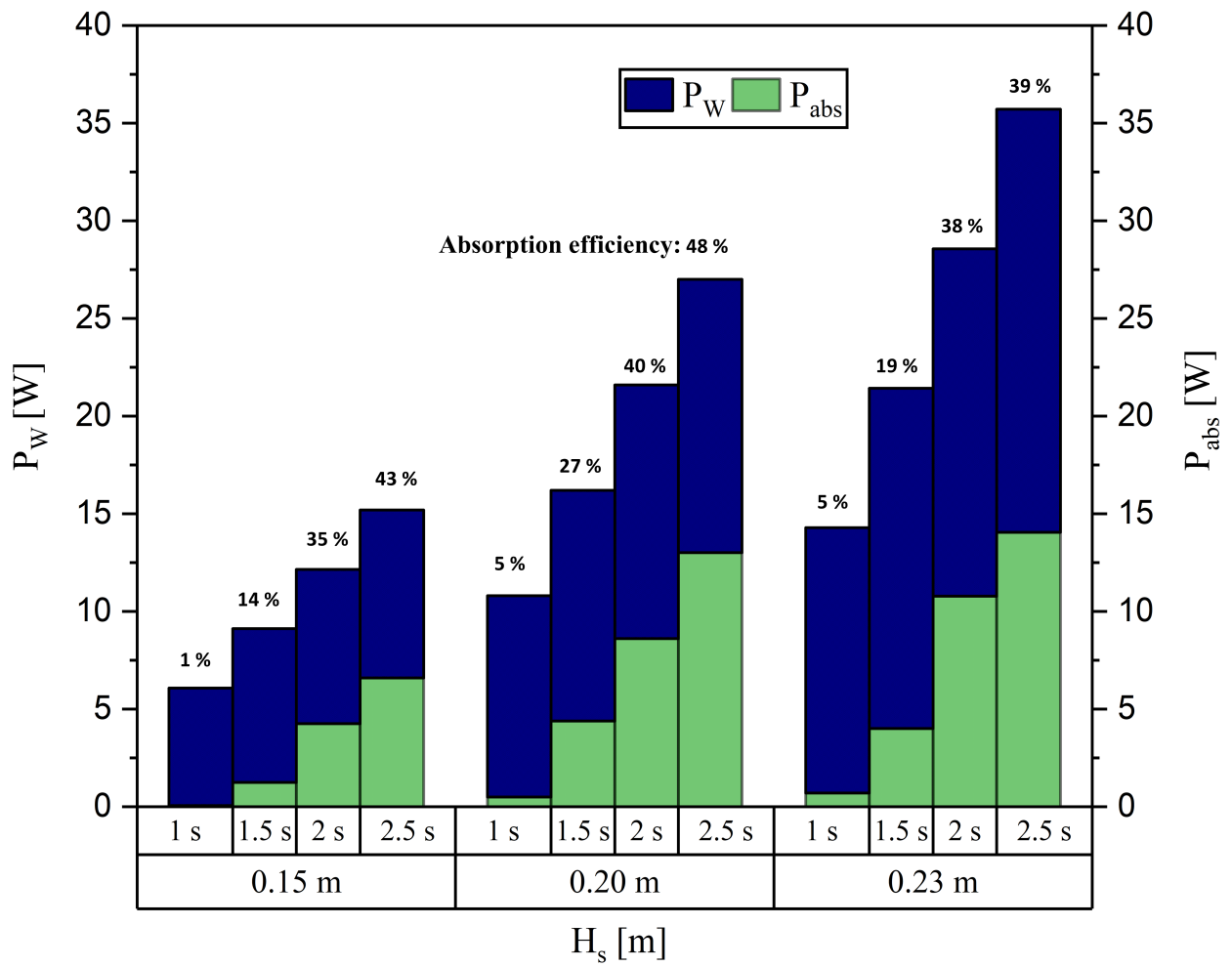
Fig. 17: Available and absorbed power for the F1A ($C_{\mathrm{PTOS}} = 100$ N·s/m).
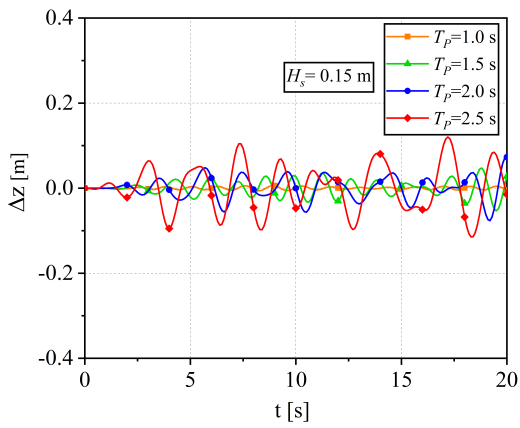
(a) $H_s = 15\,\text{cm}$
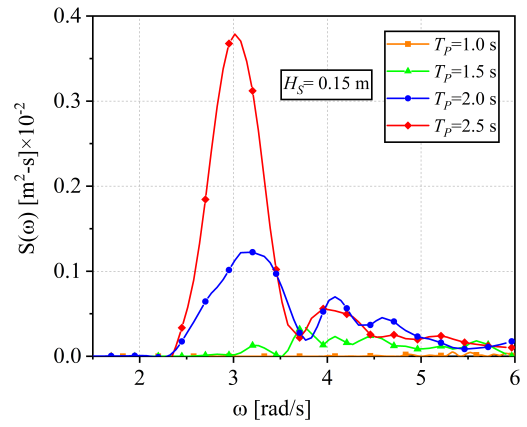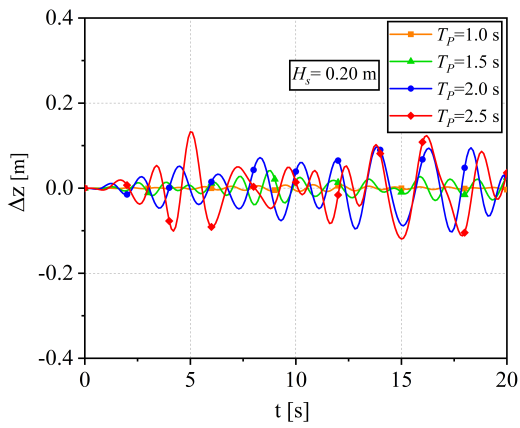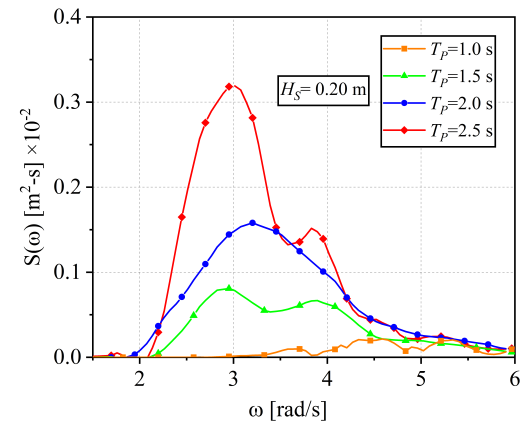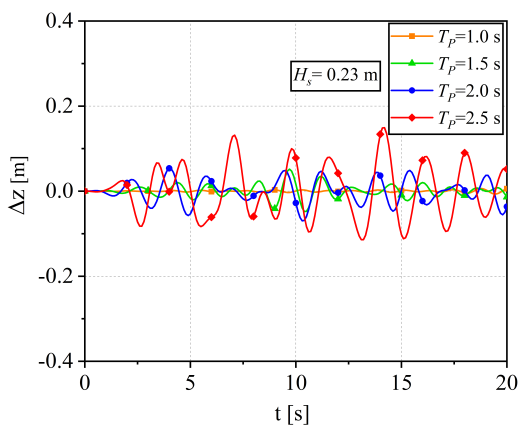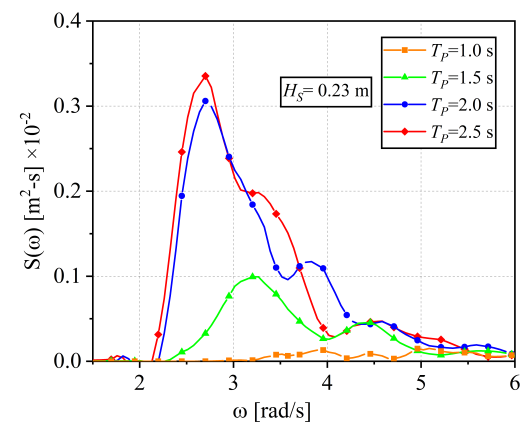
(b) $H_s = 20\,\text{cm}$

(c) $H_s = 23\,\text{cm}$

Fig. 18: Heave relative displacement for different wave heights: (a) $H_s = 15\,\text{cm}$, (b) $H_s = 20\,\text{cm}$, and (c) $H_s = 23\,\text{cm}$.

(a) $H_s = 15\,\text{cm}$

(b) $H_s = 20\,\text{cm}$

(c) $H_s = 23\,\text{cm}$

Fig. 19: Power spectral density (PSD) of relative displacement response in heave for different wave heights: (a) $H_s = 15\,\text{cm}$, (b) $H_s = 20\,\text{cm}$, and (c) $H_s = 23\,\text{cm}$.
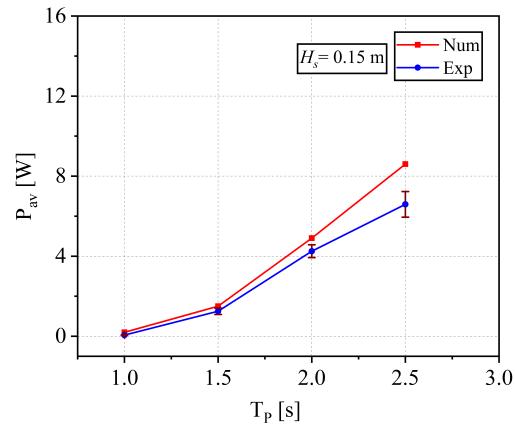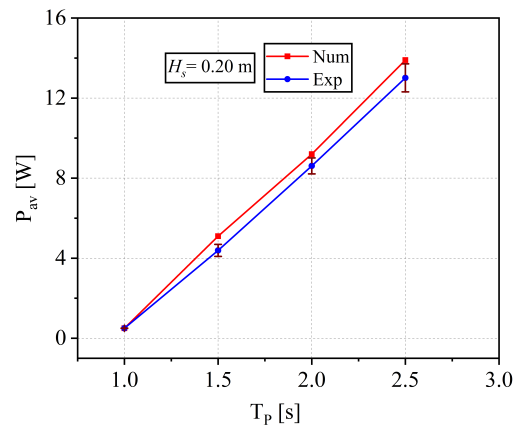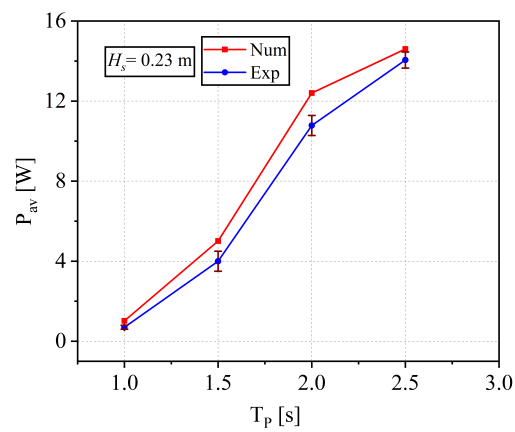
(a) $H_s = 15\,\text{cm}$

(b) $H_s = 20\,\text{cm}$

(c) $H_s = 23\,\text{cm}$

Fig. 20: Comparison of numerical and experimental results for different wave conditions: (a) $H_s = 15\,\text{cm}$, (b) $H_s = 20\,\text{cm}$, and (c) $H_s = 23\,\text{cm}$.

VI. Conclusion

This paper presents experimental and numerical analyses to investigate the hydrodynamic performance of an a multibody with an attached damper plate under irregular waves. Dynamic parameters such as the acceleration, wave load, and incoming wave characteristics were measured experimentally. Finally, the numerical and experimental powers are compared.

- A multi-body PA equipped with a damper plate was designed and tested in a wave basin in irregular wave conditions.
- Hydrodynamic coefficients were calculated using the panel method, and absorbed powers for various sea states were studied.
- The PA configuration with a damper plate (F1A) exhibited better power absorption compared to a buoy with a deeper draft (F1B), especially at higher wave heights.
- The dry bench test showed an inverse relationship between resistive load and effective PTOS damping of the PA.
- The buoy with a damper plate absorbs maximum power of 14.05 W corresponding to a significant wave height of 0.23 m and peak period of 2.5 s in the experiments.
- Maximum absorption efficiency was 48.2% at H_s = 0.2 m and T_P = 2.5 s.

Further studies are underway for sea trials to validate device performance and survivability under real ocean conditions, as well as whole-system design and optimization. Future work will also address array deployment and the hydrodynamic interactions that may affect overall energy capture.

References

[1] S. A. Sannasiraj and V. Sundar, "Assessment of wave energy potential and its harvesting approach along the indian coast," *Renewable Energy*, vol. 99, pp. 398–409, 12 2016.

[2] B. Guo, T. Wang, S. Jin, S. Duan, K. Yang, and Y. Zhao, "A review of point absorber wave energy converters," *Journal of Marine Science and Engineering*, vol. 10, 10 2022.

[3] B. Azhari, F. D. Wijaya, and E. Yazid, "Performance of linear generator designs for direct drive wave energy converter under unidirectional long-crested random waves," *Energies*, vol. 14, 8 2021.

[4] A. M. Flores, A. A. M. Rodríguez, E. Mendoza, and R. Silva, "Improving the amount of captured energy of a point-absorber wec on the mexican coast," *Energies*, vol. 17, 4 2024.

[5] X. Chen, Y. Lu, S. Zhou, and W. Chen, "Design, modeling and performance analysis of a deformable double-float wave energy converter for auvs," *Energy*, vol. 292, 4 2024.

[6] Z. Luan, B. Chen, R. Jin, G. He, H. Ghassemi, and P. Jing, "Validation of a numerical wave tank based on overset mesh for the wavestar-like wave energy converter in the south china sea," *Energy*, vol. 290, 3 2024.

[7] S. K. Natarajan and I. Cho, "New strategy on power absorption of a concentric two-body wave energy converter," *Energies*, vol. 16, no. 9, p. 3791, 2023. [Online]. Available: https://www.mdpi.com/1996-1073/16/9/3791

[8] L. Pavlidou and D. C. Angelides, "A novel two-objective optimization computational framework for a two-body heaving wave energy converter," *Renewable Energy*, vol. 191, pp. 510–534, 2022. [Online]. Available: https://doi.org/10.1016/j.renene.2022.04.006

[9] S. Kalidoss and A. Banerjee, "Site-specific modeling of self-reacting point absorber in real wave spectrum," *Ocean Engineering*, vol. 238, p. 109736, 2021.

[10] V. Vijayasankar, S. Kumar, A. Samad, and L. Zuo, "Analysis of an innovative compact point absorber wave energy converter concept suitable for small-scale power applications," *Physics of Fluids*, vol. 35, 9 2023.

[11] H. Ding, J. Zang, P. Jin, D. Ning, X. Zhao, Y. Liu, C. Blenkinsopp, and Q. Chen, "Optimization of the hydrodynamic performance of a wave energy converter in an integrated cylindrical wave energy converter-type breakwater system," *Journal of Offshore Mechanics and Arctic Engineering*, vol. 145, 10 2023.

[12] I. Yang, T. Tezdogan, and A. Incecik, "Numerical investigations of a pivoted point absorber wave energy converter integrated with breakwater using cfd," *Ocean Engineering*, vol. 274, 4 2023.

[13] M. Masoomi, H. Sarlak, and K. Rezanejad, "Hydrodynamic performance analysis of a new hybrid wave energy converter system using openfoam," *Energy*, vol. 269, 4 2023.

[14] M. A. Shabara and O. Abdelkhalik, "Dynamic modeling of the motions of variable-shape wave energy converters," *Renewable and Sustainable Energy Reviews*, vol. 173, 3 2023.

[15] T. Yu, T. Li, H. Shi, Z. Zhang, and X. Chen, "Experimental investigation on the wave-oscillating buoy interaction and wave run-up on the buoy," *Ocean Engineering*, vol. 270, 2 2023.

[16] D. R. Lande-Sudall, J. Nyland, T. R. Rykkje, P. K. Stansby, and T. Impelluso, "Hydrodynamic modelling of a multi-body wave energy converter using the moving frame method," *Marine Structures*, vol. 87, 1 2023.

[17] M. A. Jalani, M. R. Saad, M. K. H. Samion, Y. Imai, S. Nagata, and M. R. A. Rahman, "Numerical study on a hybrid wec of the backward bent duct buoy and point absorber," *Ocean Engineering*, vol. 267, 1 2023.

[18] A. Rahimi, S. Rezaei, J. Parvizian, S. Mansourzadeh, J. Lund, R. Hssini, and A. Düster, "Numerical and experimental study of the hydrodynamic coefficients and power absorption of a two-body point absorber wave energy converter," *Renewable Energy*, vol. 201, pp. 181–193, 12 2022.

[19] X. Li, D. Martin, B. Jiang, S. Chen, K. Thiagarajan, R. G. Parker, and L. Zuo, "Analysis and wave tank verification of the performance of point absorber wecs with different configurations," *IET Renewable Power Generation*, vol. 15, pp. 3309–3318, 2021. [Online]. Available: https://doi.org/10.1049/rpg2.12253

[20] C. J. Rusch, T. R. Mundon, B. D. Maurer, and B. L. Polagye, "Hydrodynamics of an asymmetric heave plate for a point absorber wave energy converter," *Ocean Engineering*, vol. 215, p. 107915, 2020. [Online]. Available: https://doi.org/10.1016/j.oceaneng.2020.107915

[21] G. Giorgi, J. Davidson, G. Habib, G. Bracco, G. Mattiazzo, and T. Kalmár-Nagy, "Nonlinear dynamic and kinematic model of a spar-buoy: Parametric resonance and yaw numerical instability," *Journal of Marine Science and Engineering*, vol. 8, no. 7, p. 504, 2020.

[22] F. Meng, A. Rafiee, B. Ding, B. Cazzolato, and M. Arjomandi, "Nonlinear hydrodynamics analysis of a submerged spherical point absorber with asymmetric mass distribution," *Renewable Energy*, vol. 147, pp. 1895–1908, 2020. [Online]. Available: https://doi.org/10.1016/j.renene.2019.09.101

[23] M. Faizal, M. R. Ahmed, and Y. H. Lee, "A design outline for floating point absorber wave energy converters," 2014.

[24] X. Zhang and J. Yang, "Power capture performance of an oscillating-body wec with nonlinear snap through pto systems in irregular waves," *Applied Ocean Research*, vol. 52, pp. 261–273, 8 2015.

[25] Y.-H. Yu and K. Ruehl, "Wec-sim training course for users and developers foswec wave tank testing and wec-sim simulation," 2004.

[26] J. J. Jensen, "Ocean waves," in *Load and Global Response of Ships*, ser. Elsevier Ocean Engineering Series. Elsevier, 2001, pp. 43–122.

[27] Ansys, *Ansys AQWA theory manual*, Canonsburg, PA, USA, 2012. [Online]. Available: https://ansyshelp.ansys.com/public/account/secured?returnurl=//Views/Secured/prod_page.html?pn=Aqwa&prodver=24.2&lang=en

[28] Y. Ma, A. Zhang, L. Yang, H. Li, Z. Zhai, and H. Zhou, "Motion simulation and performance analysis of two-body floating point absorber wave energy converter," *Renewable Energy*, vol. 157, pp. 353–367, 9 2020.

[29] W. Koo and J. D. Kim, "Simplified formulas of heave added mass coefficients at high frequency for various two-dimensional bodies in a finite water depth," *International Journal of Naval Architecture and Ocean Engineering*, vol. 7, pp. 115–127, 2015.

[30] R. Waters, M. Stålberg, O. Danielsson, O. Svensson, S. Gustafsson, E. Strömstedt, M. Eriksson, J. Sundberg, and M. Leijon, "Experimental results from sea trials of an offshore wave energy system," *Applied Physics Letters*, vol. 90, 2007.